JBC RESEARCH ARTICLE

Isocitrate dehydrogenase 3b is required for spermiogenesis but dispensable for retinal viability

Received for publication, May 11, 2022, and in revised form, August 8, 2022 Published, Papers in Press, August 17, 2022,
https://doi.org/10.1016/j.jbc.2022.102387

Siyan Zhu[1,2,3], Jiancheng Huang[1,2,4,5], Rong Xu[1,2], Yekai Wang[1,2], Yiming Wan[6], Rachel McNeel[1,2], Edward Parker[7], Douglas Kolson[1], Michelle Yam[1,2], Bradley Webb[2], Chen Zhao[4,5], Jenna Sigado[1,2], and Jianhai Du[1,2,*]

From the [1]Department of Ophthalmology and Visual Sciences, [2]Department of Biochemistry, and [3]Department of Pharmaceutical and Pharmacological Science, West Virginia University, Morgantown, West Virginia, USA; [4]Eye Institute, Eye & ENT Hospital, Shanghai Medical College, Fudan University, Shanghai, China; [5]NHC Key Laboratory of Myopia (Fudan University), Key Laboratory of Myopia, Chinese Academy of Medical Sciences, and Shanghai Key Laboratory of Visual Impairment and Restoration (Fudan University), Shanghai, China ;[6]Department of Biomedical Engineering Department, Stony Brook University, Stony Brook, New York, USA; [7]Department of Ophthalmology, University of Washington, Seattle, Washington, USA

Edited by Ruma Banerjee

Isocitrate dehydrogenase 3 (IDH3) is a key enzyme in the mitochondrial tricarboxylic acid (TCA) cycle, which catalyzes the decarboxylation of isocitrate into α-ketoglutarate and concurrently converts NAD^+ into NADH. Dysfunction of IDH3B, the β subunit of IDH3, has been previously correlated with retinal degeneration and male infertility in humans, but tissue-specific effects of IDH3 dysfunction are unclear. Here, we generated *Idh3b*-KO mice and found that IDH3B is essential for IDH3 activity in multiple tissues. We determined that loss of *Idh3b* in mice causes substantial accumulation of isocitrate and its precursors in the TCA cycle, particularly in the testes, whereas the levels of the downstream metabolites remain unchanged or slightly increased. However, the *Idh3b*-KO mice did not fully recapitulate the defects observed in humans. Global deletion of *Idh3b* only causes male infertility but not retinal degeneration in mice. Our investigation showed that loss of *Idh3b* causes an energetic deficit and disrupts the biogenesis of acrosome and flagellum, resulting in spermiogenesis arrestment in sperm cells. Together, we demonstrate that IDH3B controls its substrate levels in the TCA cycle, and it is required for sperm mitochondrial metabolism and spermiogenesis, highlighting the importance of the tissue-specific function of the ubiquitous TCA cycle.

The mitochondrial tricarboxylic acid (TCA) cycle is a central metabolic pathway for energy production, macromolecule synthesis, cellular redox balance, and cell signaling (1). This cycle consists of a series of biochemical reactions to oxidize nutrients to generate ATP and intermediates for the synthesis of proteins, lipids, and nucleotides. Beyond these classical functions, mitochondrial intermediates, such as citrate, α-ketoglutarate (αKG), and succinate, are also important signaling molecules for post-translational modifications and epigenetic control of gene expression (1, 2). The malfunction of the TCA cycle is implicated in a wide spectrum of disorders, including neurodegenerative diseases, blindness, tumorigenesis, inflammation, obesity, and male infertility (1, 3–5).

Isocitrate dehydrogenase (IDH), which converts isocitrate into αKG, is a crucial control point for the TCA cycle. In mammalians, IDH exists in three isoforms: IDH1, IDH2, and IDH3. IDH1 and IDH2, localized in the cytosol and mitochondria, respectively, catalyze the reversible interconversion of isocitrate and αKG using $NADP(H)^+$ as cofactor. Their forward reaction (oxidative decarboxylation) and reverse reaction (reductive carboxylation) play critical roles in lipogenesis, redox homeostasis, and cell proliferation (6–9). IDH3 is the classic TCA cycle enzyme, using NAD^+ as its cofactor to catalyze the irreversible conversion of isocitrate into αKG and the reduction of NAD^+ into NADH for mitochondrial respiration. IDH3 finely regulates the rate of the TCA cycle through substrate availability and allosteric regulation. IDH3 activity is stimulated by citrate, isocitrate, NAD^+, ADP, Mg^{2+}, Mn^{2+}, and Ca^{2+} but inhibited by NADH, αKG, ATP, and NADPH (6, 10–12).

IDH3 is a heterotetramer composed of the αβ and αγ heterodimers. The α subunit is critical for the catalytic activity, but it requires the β and γ subunits for structural assembly and allosteric regulation. Without β or γ subunit, the α subunit alone has almost no activity (13, 14). IDH3 subunits are encoded by *IDH3A*, *IDH3B*, and *IDH3G*, which express abundantly in mitochondria-rich tissues, such as the heart, skeletal muscle, and brain. Although ubiquitously expressed, human mutations or altered expression of IDH subunits are biased toward specific tissues in diseases. Mutations of *IDH3A* and *IDH3B* are identified in patients with inherited retinal degeneration, pseudocoloboma, and epileptic encephalopathy (4, 15–18). *IDH3A* is associated with tumorigenesis, and its expression is upregulated in patient samples from hepatocellular carcinoma and glioblastoma (19, 20). Significantly, reduced IDH3B is found in spermatozoa from patients with male infertility and poor sperm motility (5, 21, 22). Loss of *Idh3a* in mice is embryonic lethal, but mice with *Idh3a* E229K

* For correspondence: Jianhai Du, jianhai.du@hsc.wvu.edu.

mutation exhibits retinal degeneration (23). In *Drosophila melanogaster*, *Idh3b*-mutant larval salivary gland cells fail to undergo mitochondrial fragmentation and oxidative phosphorylation, resulting in the death of these cells (24). Although the enzyme structure, regulation, and mutations have been well studied, how mutations or altered expression of IDH3 subunits impact mitochondrial metabolism to cause tissue-specific impairment *in vivo* remains elusive.

In this study, we investigate how the global loss of *Idh3b* influences mitochondrial metabolism, visual function, retinal viability, and male fertility in mice. We demonstrate that IDH3B is essential for IDH3 activity and TCA cycle intermediate metabolism. Surprisingly, testis mitochondria specifically rely on IDH3 for their mitochondrial metabolism, and the loss of *Idh3b* leads to severe arrestment of spermiogenesis. However, IDH3B is dispensable for visual function and retinal viability. Our study provides fundamental information on the tissue-specific function and metabolic regulation of IDH3 and sheds new insight on understanding the role of the TCA cycle in retinal health, sperm development, and male infertility.

Results

Global deletion of IDH3B reduces or abolishes IDH3 activity in the heart, brain, retina, and testes

To determine the functions of IDH3B *in vivo*, we obtained *Idh3b* global (whole-body) KO mice from the Jackson Laboratory. The *Idh3b*-KO mice were generated by the injection of four guide RNAs using CRISPR/Cas9 technology, resulting in 343 bp deletion in exons 2 to 4 (Fig. 1*A*). Before validating the deletion of IDH3B, we evaluated the protein levels of IDH3 subunits in different tissues from the WT mice by Western blot. Among the eight tissues we examined, the heart and brain were the two tissues with the most abundant IDH3B expression (Fig. 1*B*). To confirm the global deletion of *Idh3b* in mice, we chose four tissues for analyses: tissues with the most abundant IDH3B protein expression (heart and brain) and tissues with potential functional defects based on the literature (retina and testis). Immunoblot results showed that IDH3B protein level is similar between the heterozygous (HET) and the WT mice in all the four tissues but undetectable in the homozygous (KO) mice, confirming that IDH3B is globally deleted in the KO mice (Fig. 1*C*). To examine how IDH3 activity is affected when IDH3B is absent, we performed enzyme activity assays for retina, brain, heart, and testis from WT, HET, and KO mice. IDH3 activities in the retina, brain, and testis from the KO mice were almost completely abolished; however, ∼30% of IDH3 activity was preserved in the heart (Fig. 1*D*). Since the HET mice had similar IDH3B protein level and IDH3 activities to the WT, we adapted the HET mice as the control group for most analyses to save animals and facilitate breeding. Taken together, we validated the global deletion of IDH3B in *Idh3b*-KO mice and showed that IDH3B is essential for IDH3 activity, especially in the retina, brain, and testis.

Loss of Idh3b changes the expression levels of IDH3A and IDH3G subunits in testis but not retina

To investigate whether the loss of *Idh3b* altered the expression of other IDH3 subunits, we quantified the protein expression of IDH3A and IDH3G in the retina and testis. In the retina, densitometry data showed no significant difference in IDH3A and IDH3B protein levels between HET and KO (Fig. 1, *E–G*). However, in the testis, IDH3A was reduced by 75% ($p < 0.05$), whereas IDH3G was increased by 35% ($p < 0.05$) in the KO mice (Fig. 1, *H–J*). Overall, our results suggest that IDH3B is required for the proper expression of other IDH3 subunits in the testis but not the retina.

Idh3b KO mice have normal growth and vision without retinal degeneration

The *Idh3b*-KO mice showed normal appearance, hair color, and body weight (Fig. S1, *A* and *B*). There was no difference in the tissues/body weight in major organs, including heart, kidney, and liver between the KO and HET mice, suggesting that *Idh3b*-KO mice have normal body growth (Fig. S1, *C–E*). To investigate whether the KO mice have retinal degeneration, we examined the visual function by electroretinogram (ERG) and retinal morphology by optical coherence tomography (OCT) *in vivo* and H&E staining of eye sections *in vitro*. ERG responses from postnatal day 115 (P115) to P250 progressively declined with aging at the same rate between the KO and HET mice (Fig. S2, *A–D*). At P250, there were no significant changes in scotopic and photopic a-wave and b-wave at all light intensities in KO mice, compared with the HET (Fig. 2, *A–D*). OCT showed no difference in the thickness of each retinal layer between the KO and HET mice at the age of P200 (Fig. S2, *E* and *F*). Quantification of the thickness of the photoreceptor layer (outer segment and inner segment) and the number of nuclei in outer nuclei layer from H&E-stained eye sections confirmed that *Idh3b*-KO mice had normal retinal morphology at P250 (Fig. 2, *E–H*). Together, these results demonstrate that *Idh3b*-KO mice have normal vision and retinal morphology without retinal degeneration.

The substrates of the IDH3 reaction are accumulated, but the products remain unchanged in Idh3b KO retinas

IDH3 irreversibly converts isocitrate from citrate and aconitate into αKG in the TCA cycle (Fig. 3*A*). To examine how *Idh3b* ablation affects mitochondrial intermediary metabolism, we measured the abundance of TCA cycle metabolites from freshly isolated mouse retinas using GC/MS. As expected, metabolites from upstream reactions of IDH3, including citrate, isocitrate, and aconitate, were accumulated about twofold in retinas from the KO mice (Fig. 3*B*). However, αKG and its downstream metabolites, including glutamate, succinate, fumarate, malate, and aspartate, remained unchanged (Fig. 3*B*). These TCA cycle metabolites can be generated from different nutrient sources, such as glucose, fatty acids, and amino acids. To trace the changes of metabolites from the same nutrient source, we incubated freshly

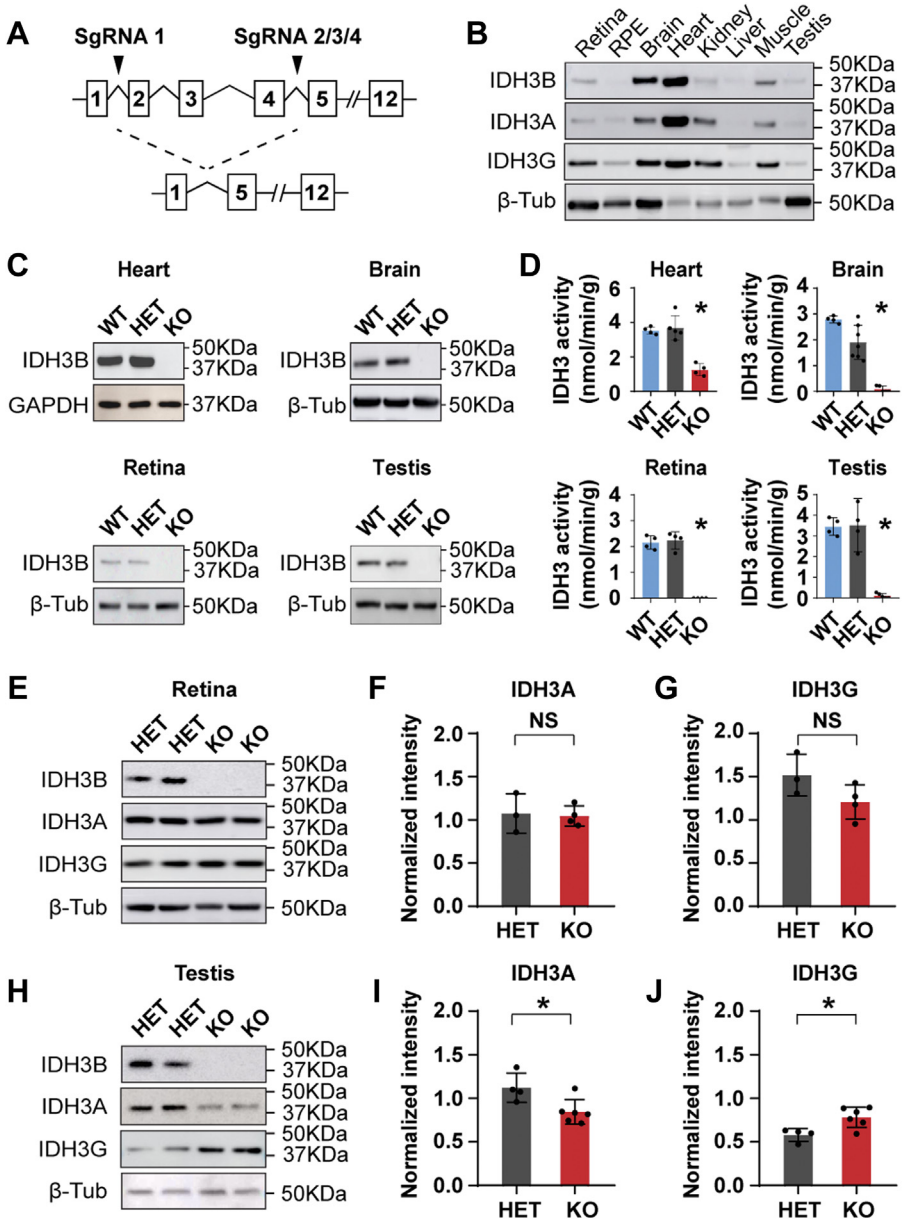

Figure 1. Generation of *Idh3b* KO mice. *A*, schematic of *Idh3b*-KO mice with a deletion of exon 2 to 4 by CRISPR/Cas9. *B*, protein expression of IDH3A, IDH3B, and IDH3G in retina, retinal pigmented epithelium (RPE), brain, heart, kidney, liver, muscle, and testis from WT mice at P80. *C*, Western blot analysis for IDH3B in heart, brain, retina, and testis from WT, HET, and KO mice. GAPDH was used as loading control for heart and β-tubulin (β-tub) was used as loading control for brain, retina, and testis. Repeated for three times. *D*, enzymatic activity analysis of IDH3 in heart, brain, retina, and testis from WT, HET, and KO mice at P50. N ≥ 4. *$p < 0.05$ KO *versus* WT or HET. *E–G*, Western blot analysis of IDH3A and IDH3G expression in retinas from mice at P200. *E*, representative Western blot image. *F* and *G*, semiquantification of blots by normalizing with the loading control β-tubulin. N ≥ 3, *$p < 0.05$. *H–J*, Western blot analysis of IDH3A and IDH3G expression in testis from mice at P50. *H*, representative Western blot image. *I* and *J*, semiquantification of blots. N ≥ 4, *$p < 0.05$. Data are all represented as mean ± SD; *t* test. HET, heterozygous; IDH, isocitrate dehydrogenase.

isolated retinas with ^{13}C glucose and analyzed ^{13}C glucose-labeled metabolites by GC/MS as previously reported (25, 26). Our results showed that the abundance of ^{13}C glucose-labeled glycolytic intermediates including phosphoenolpyruvate, pyruvate, and lactate were similar between the HET and KO retinas. For TCA cycle intermediates, ^{13}C glucose-labeled citrate, isocitrate, and aconitate increased twofold to threefold in the KO retinas, whereas other intermediates remained unchanged (Fig. 3*C*). These results suggest that IDH3B is critical for the levels of its substrates but not products. To examine whether another two IDH isoenzymes (IDH1 and IDH2) compensated for the loss of IDH3B, we measured their protein expression and enzyme activity from the isolated retinas. There was no significant difference in either IDH1 or IDH2 expression level between HET and KO (Fig. 3, *D–F*). The retinas from HET and KO showed similar NADP-dependent IDH activity from IDH1 and IDH2 (Fig. 3*G*). Overall, these results indicate that IDH3B is essential for mitochondrial isocitrate oxidation in the retina and for maintaining the levels of TCA cycle metabolites.

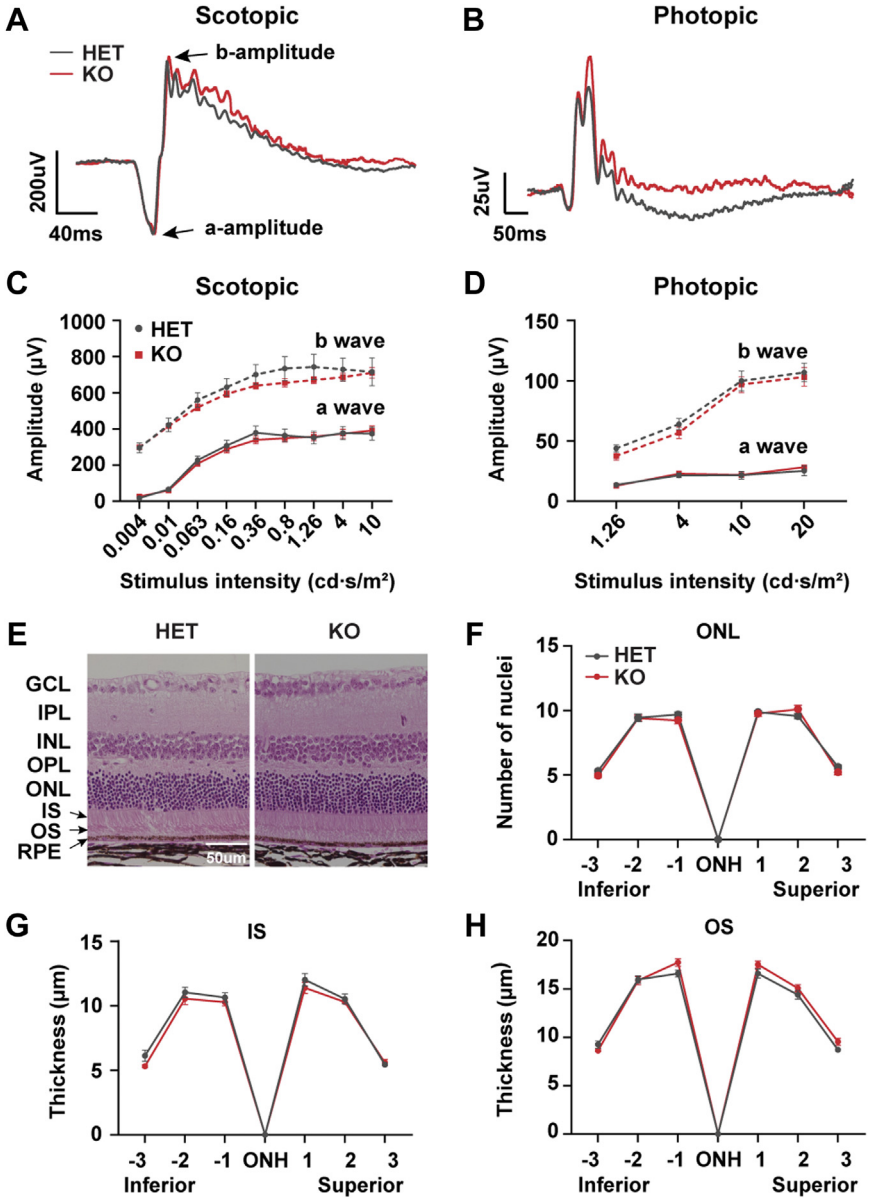

Figure 2. Loss of *Idh3b* did not affect visual function and retinal health in mice. *A* and *B*, representative scotopic (0.8 cd*s/m^2) and photopic (10 cd*s/m^2) ERGs of *Idh3b* KO and *Idh3b* HET (control) at P250. N ≥ 4. *C* and *D*, scotopic ERG and photopic ERG analysis under different light intensities for HET and KO mice at P250. N ≥ 4. *E*, representative retinal H&E images from HET and KO mice at P250. *F*, number of nuclei in outer nuclei layer (ONL) at different positions of the eye. N ≥ 3. *G* and *H*, thickness of inner segment (IS) and outer segment (OS) at different positions of the eye. N ≥ 3. Data are all represented as mean ± SD; *t* test. ERG, electroretinogram; HET, heterozygous.

Idh3b KO male mice are sterile with no matured sperms in the epididymis

During the generation of *Idh3b*-KO mice, we observed that male KO mice could not generate pups when bred with either HET females or WT females for up to 6 months. However, the breeding of KO females with HET males was normal. We performed a gross examination of isolated testes and found that the size and weight of testes is similar between the HET and KO (Fig. S3, *A* and *B*). To ask whether the sperms were normal in *Idh3b*-KO mice, we dissected the cauda epididymis (where matured sperms are stored), live-imaged, and counted the number of sperm cells under the light microscope. All sperm cells from the HET mice were motile with normal head–tail morphology (Fig. 4*A* and Video S1). However, the KO mice had nearly no mature spermatozoa and showed a large accumulation of immotile round sperm cells (Fig. 4*B* and Video S2). By counting the sperm cells, we found that both WT and HET mice had ∼6 million healthy and mature spermatozoa, whereas the KO mice had no mature spermatozoa except ∼0.8 million round sperm cells (Fig. 4, *C* and *D*). Histological analysis of the cauda epididymis using H&E staining confirmed that epididymal ducts in the KO mice were filled with immature round sperm cells (Fig. 4, *E* and *F*). These immature cells exhibited multiple defects including enlarged and vacuolated cytoplasm, vacuolated nucleus, multinucleation, and fragmentation (Fig. 4,*E*' and *F*'). Overall, we

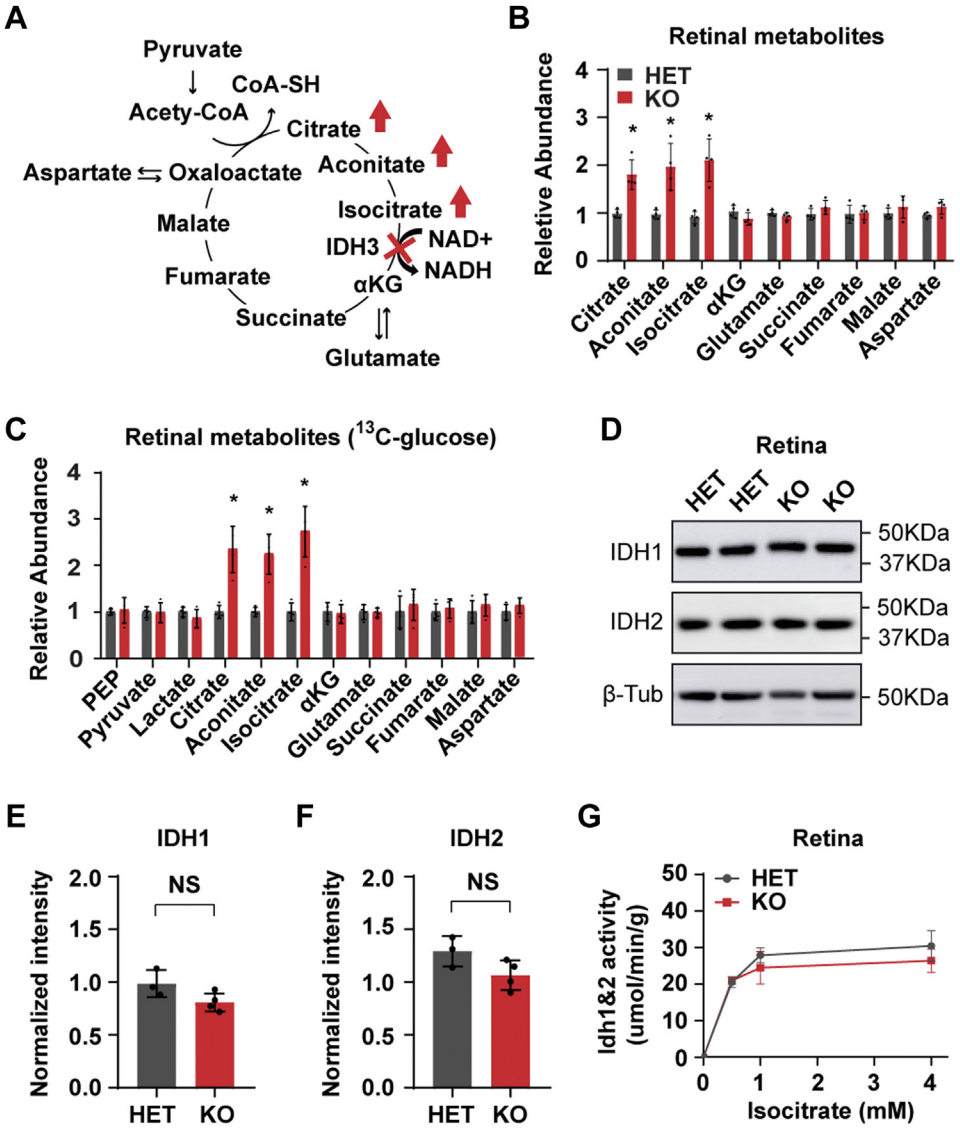

Figure 3. Loss of *Idh3b* disrupted cellular metabolism in the retina. *A*, schematic of TCA cycle metabolism. *B*, fold change of TCA cycle metabolites in retina from KO mice. N = 4, $*p < 0.05$. *C*, fold change of ^{13}C-glucose-derived metabolites in the retina from KO mice. N ≥ 4, $*p < 0.05$. *D–F*, Western blot analysis of IDH1 and IDH2 in the retina from mice at P200. *D*, representative Western blot image. *E* and *F*, semiquantification of IDH1 and IDH2 level in retina. β-Tubulin (β-Tub) was used as loading control. N ≥ 3. *G*, enzymatic activity of IDH1 and IDH2 under different isocitrate concentrations in the retina from HET and KO mice. N ≥ 4. HET, heterozygous; IDH, isocitrate dehydrogenase; TCA, tricarboxylic acid.

found that *Idh3b*-KO male mice were infertile without mature spermatozoa, indicating that sperm development is impaired in the *Idh3b*-KO mice.

Spermiogenesis is arrested in Idh3b KO mice

Sperm development occurs in seminiferous tubules of the testis and consists of three stages: mitosis, meiosis, and spermiogenesis. To investigate how *Idh3b* ablation influenced sperm development, we stained cross-sectioned testis and quantified different cell populations in seminiferous tubules. There was no difference in the number of cells in the early developmental stages, including spermatogonia, pachytene, leptotene/zygotene, and spermatid, between the HET and KO mice (Fig. 5, *A–C*), suggesting that sperm cells have normal development in mitosis and meiosis in the KO mice. However, the number of mature spermatozoa was reduced approximately fivefold in the KO testis, indicating a spermiogenesis arrestment in *Idh3b*-KO mice (Fig. 5*C*). Mouse spermiogenesis can be subdivided into 16 steps based on the morphological changes of the acrosome, a cap-like organelle attached to the nucleus (Fig. S4*A*). To define the impaired steps in spermiogenesis in the KO mice, we stained the glycoprotein in acrosome by periodic acid-Schiff. We found that spermatids at the same differential step orderly encircled the seminiferous tubules in HET testis but were disorganized in the KO testis (Fig. S4*B*). Detached or malformed acrosomes were observed in KO but not HET in steps 2 to 7 (Fig. 5, *D–I*). HET mice developed a normal oval shape nucleus starting from step 8 (Fig. 5, *J–L*). However, the shapes of the nucleus in the KO testis were irregular with round heads (Fig. 5 *K–M*). In addition, flagella (the tails), another important feature in mature

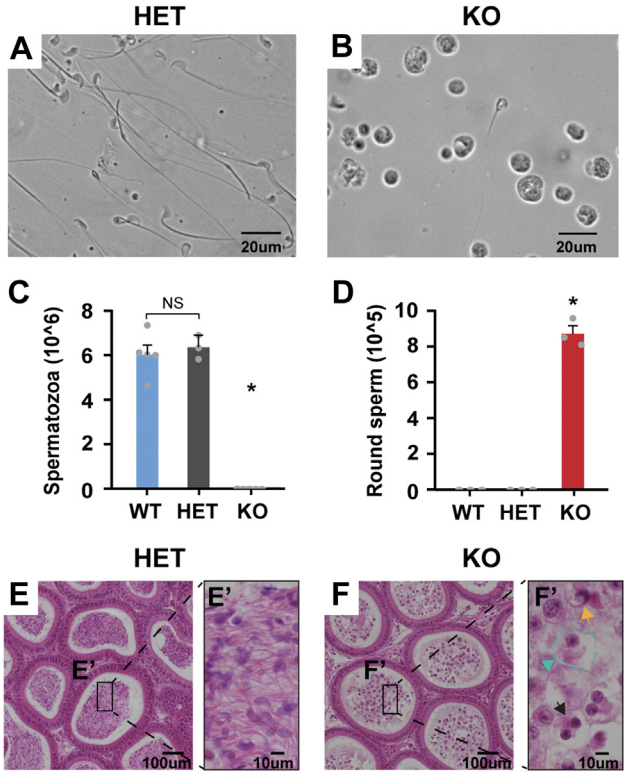

Figure 4. *Idh3b* male KO mice are sterile and lack the ability to produce mature spermatozoa. *A* and *B*, representative images of sperm cells obtained from the cauda epididymis of HET and KO mice at P50. *C* and *D*, quantifications of mature spermatozoa and round sperm cells in the cauda epididymis. N ≥ 3, $*p < 0.05$ *versus* WT or HET. Data are represented as mean ± SD; *t* test. *E* and *F*, H&E analysis of cauda epididymis in HET and KO mice at P50. *E′* and *F′*, magnified H&E images (*green arrow*: enlarged and vacuolated cytoplasm; *yellow arrow*: vacuolated nucleus; and *black arrow*: fragmented nucleus). HET, heterozygous.

spermatozoa, were abundant in the HET but scarce in KO mice (Fig. S4*B*). These results indicate that loss of *Idh3b* results in spermiogenesis arrestment.

Loss of IDH3B disrupts acrosome biogenesis

The acrosome is formed by organelle-derived (particularly Golgi) proacrosomal vesicles that traffick, fuse, and anchor to the nuclear surface during spermiogenesis. Acrosome biogenesis can be divided into four phases: Golgi (steps 1–3), cap (steps 4–7), acrosome (steps 8–12), and maturation (steps 13–16) phases (Fig. S4*A*). To visualize acrosome biogenesis, we stained the acrosome, nucleus, and Golgi with peptide nucleic acid, 4′,6-diamidino-2-phenylindole, and GM130. In steps 2 to 3 (Golgi phase), a single and sphere acrosomal granule is attached to the nucleus in the HET testis but detached in the KO with or without misoriented Golgi, indicating a compromised vesicle trafficking and anchoring in the KO mice (Fig. 6, *A* and *B*). In steps 4 to 5 (cap phase), proacrosomal granules displayed abnormal shapes and failed to transform into a cap shape in the KO testis (Fig. 6, *C–F*). In steps 6 to 7 (cap phase), cap-shaped proacrosomal vesicles were orderly oriented toward the nucleus in the HET, but the proacrosomal vesicles were scattered to float around the nucleus in the KO testis, indicating vesicle trafficking and fusion impairments. In the later steps (acrosome and maturation phases), the HET mice developed elongated mature acrosomes, whereas the KO acrosomes were fragmented and disoriented. (Fig. 6, *G–J*). To confirm these findings, we examined the ultrastructure of acrosome biogenesis using the transmission electron microscope (TEM). Consistently, we found multiple defects in acrosome biogenesis in the KO. These defects included (1) Golgi misorientation and acrosome detachment in Golgi phase, (2) no acrosome or eccentric and dilated acrosome granules in cap phase, (3) no acrosome or immature acrosome with mislocalized acrosomal granule in acrosome phase, and (4) no acrosome or detached acrosome in maturation phase (Fig. 6, *I–V*). To further evaluate these defects, we measured the expression of key proteins in acrosome biogenesis, including heat shock protein 90 beta family member 1 (HSP90B1), Golgi associated PDZ and coiled-coil motif containing (GOPC), and acrosomal vesicle protein 1 (ACRV1) (Fig. 6, *W–X*). HSP90B1, an endoplasmic reticulum protein required for vesicle formation (27), was similar between the KO and HET. GOPC, which is required for vesicle fusion, was also maintained with the same amount in the KO (28). Remarkably, ACRV1, an acrosomal matrix protein arising during acrosome biogenesis, was significantly decreased in testis from the KO mice (29). Together, these results strongly support that IDH3B is essential for acrosome biogenesis.

Idh3b is required for flagellum assembly

Flagellum biogenesis is another hallmark for spermiogenesis. In KO testis, we found much fewer residual bodies and flagella in the lumen of testicular tubules (Fig. 5*B′*). To investigate how flagellum formation is affected, we stained axoneme, the core structure of flagellum, with the antibody against acetyl-α-tubulin. In testicular tubules containing late-step spermatids, we found that the distal ends of flagella were well oriented toward the lumen in the HET but were misoriented and disorganized in the KO mice (Fig. 7, *A–D*). The mitochondrial sheath is an important structural component, where mitochondria align with axoneme in the flagellum. Fluorescent staining of mitochondria using MitoTracker showed substantially reduced signals in the KO sections, suggesting that the mitochondrial sheath is disrupted (Fig. 7, *E* and *F*). Fibrous sheath and outer dense fibers are crucial for the assembly and integrity of the flagellum. To quantitatively study the structural changes in the flagellum, we performed Western blot with antibodies against acetyl-tubulin (axoneme marker), A-kinase anchoring protein 4 (AKAP82) (fibrous sheath marker), and outer dense fiber 2 (ODF2) (outer dense fiber marker). Our results showed that all these proteins were significantly reduced, especially AKAP82, which was almost undetectable in the KO testis (Fig. 7, *G* and *H*). To validate these findings, we examined the ultrastructure of flagellum components using TEM. We found structural defects in all three pieces in the flagellum from the KO testis (Fig. 7, *I–R*). The mitochondrial sheath disappeared, and multiflagella were formed in the midpiece (Fig. 7, *I– K*). In the principal piece, there were abnormal axonemes and reduced longitudinal

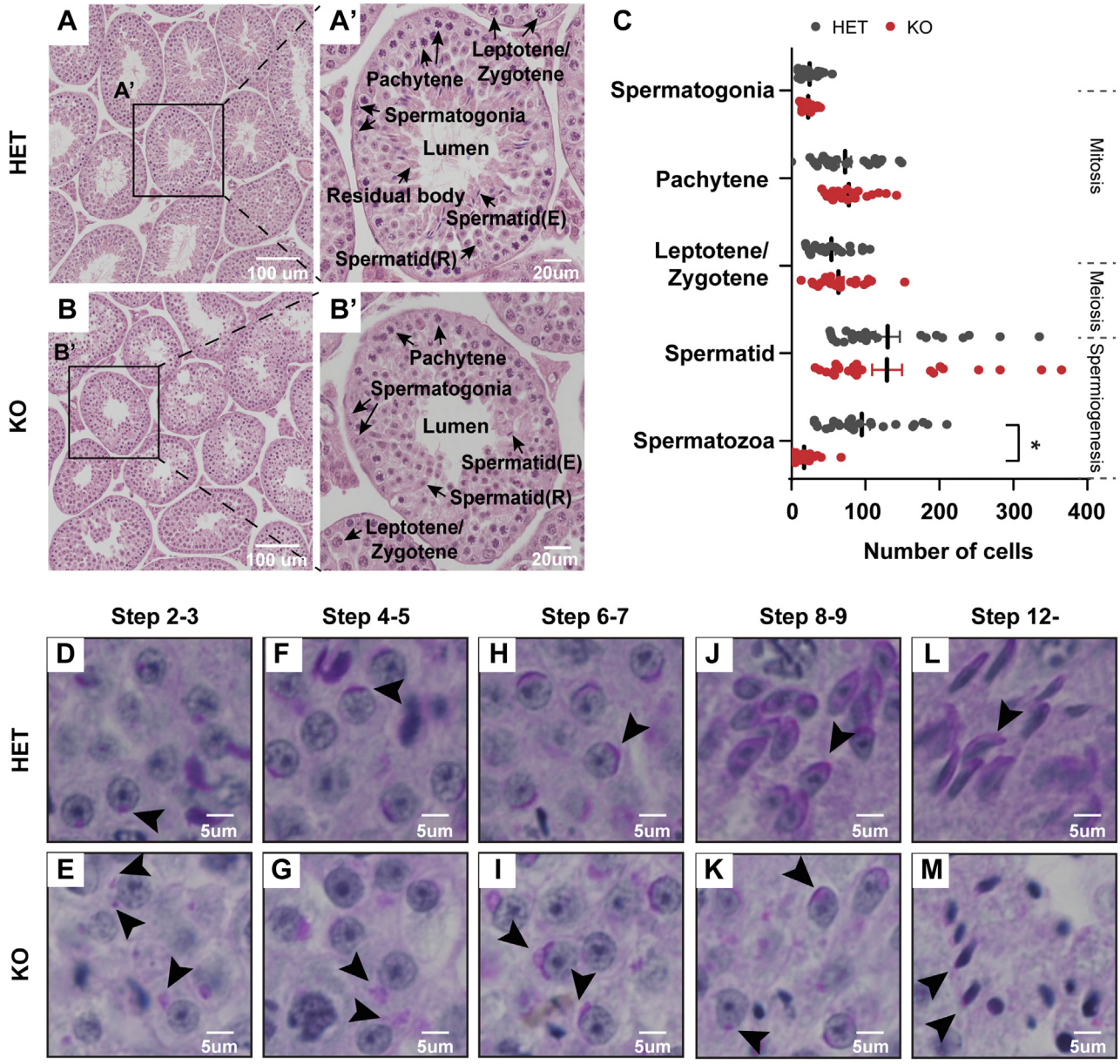

Figure 5. IDH3B is essential for spermiogenesis. *A* and *B*, representative H&E images for testicular sections from mice at P50. *A′* and *B′*, late-stage testicular tubule with mature spermatozoa. Spermatid (R): round spermatid, spermatid (E): elongated spermatid. *C*, quantification of different sperm cell populations from the HET and KO testes. N of tubules = 20, $*p < 0.05$. Data are represented as mean ± SD; *t* test. *D–M*, periodic acid–Schiff stain (PAS) for staging sperm differentiation in testes. *Arrowheads* pointed to the acrosome. HET, heterozygous; IDH3B, isocitrate dehydrogenase 3B.

columns (Fig. 7, *L–N*). In the endpiece, the plasma membrane was irregular and disorganized, which is a notable atypical feature of defected flagellum (Fig. 7, *O–Q*). Together, our results suggest that IDH3B is critical for maintaining intact flagellar structure, including axoneme, mitochondrial sheath, fibrous sheath, and outer dense fiber.

Idh3b is specifically required for testis mitochondrial metabolism

To test how the loss of IDh3b influences testis metabolism, we first measured TCA cycle metabolites as done previously with the retinas using GC/MS. Surprisingly, metabolites upstream of the IDH3 reaction, including citrate, isocitrate, and aconitate, increased 10-fold∼20-fold in testes from the KO, compared with the control (Fig. 8*A*). However, the metabolites downstream of the IDH3 reaction were either slightly increased or unchanged (Fig. 8*A*). To ask whether this massive accumulation of precursors was specific to the testes, we analyzed TCA cycle intermediates from hearts where IDH3b protein is most abundant. Similar to the retina, metabolites upstream of the IDH3 reaction in the IDH3B KO hearts increased only twofold to threefold (Fig. 8*B*). NADP-dependent IDH1 and IDH2 can also oxidize isocitrate. There was no significant difference in protein expression and enzyme activities of IDH1/2 between the HET and KO testes (Fig. S5, *A–D*). IDH1/2 activities increased with isocitrate and reached the maximal activities at ∼2 mM. These results suggest that

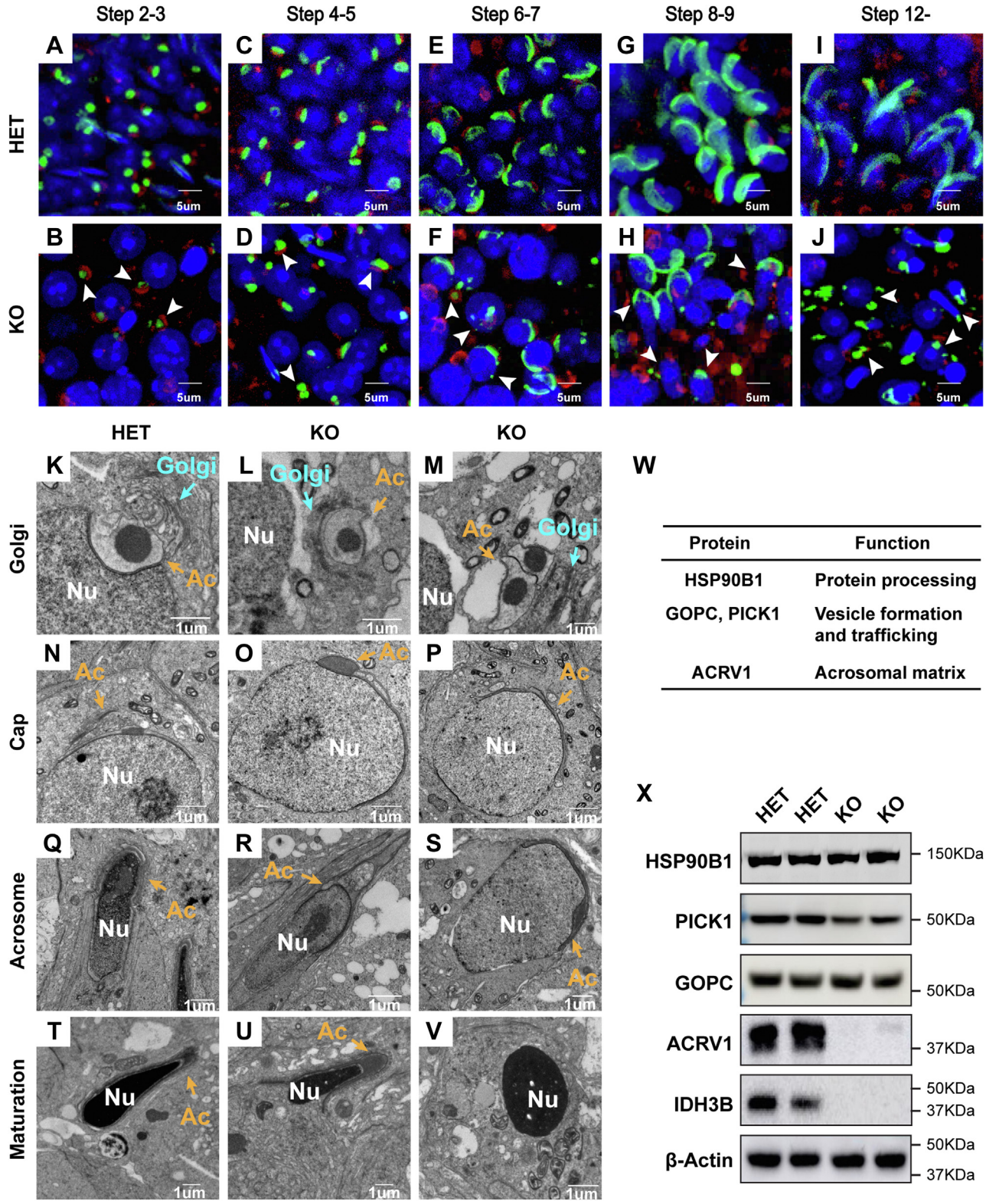

Figure 6. Acrosome biogenesis defects in *Idh3b* KO mice. *A–J*, representative images for immunofluorescent staining of acrosome and Golgi at different stages in testicular tubular sections from mice at P50. *Red*, GM130; *blue*, DAPI (4′,6-diamidino-2-phenylindole); and *green*, PNA. *Arrowhead*: defected acrosome. *K–V*, ultrastructure analysis of acrosome biogenesis at Golgi, cap, acrosome, and maturation stages. *Blue arrows*, Golgi; *yellow arrows*: acrosome (Ac), nucleus (Nu). *W*, table of proteins essential for acrosome biogenesis. ACRV1, acrosomal vesicle protein 1; GOPC, Golgi associated PDZ and coiled-coil motif; Hsp90B1, heat shock protein 90 beta family member 1; PICK1, protein interacting with PRKCA 1. *X*, Western blot analysis of listed proteins in testis from HET and KO mice at P50. HET, heterozygous.

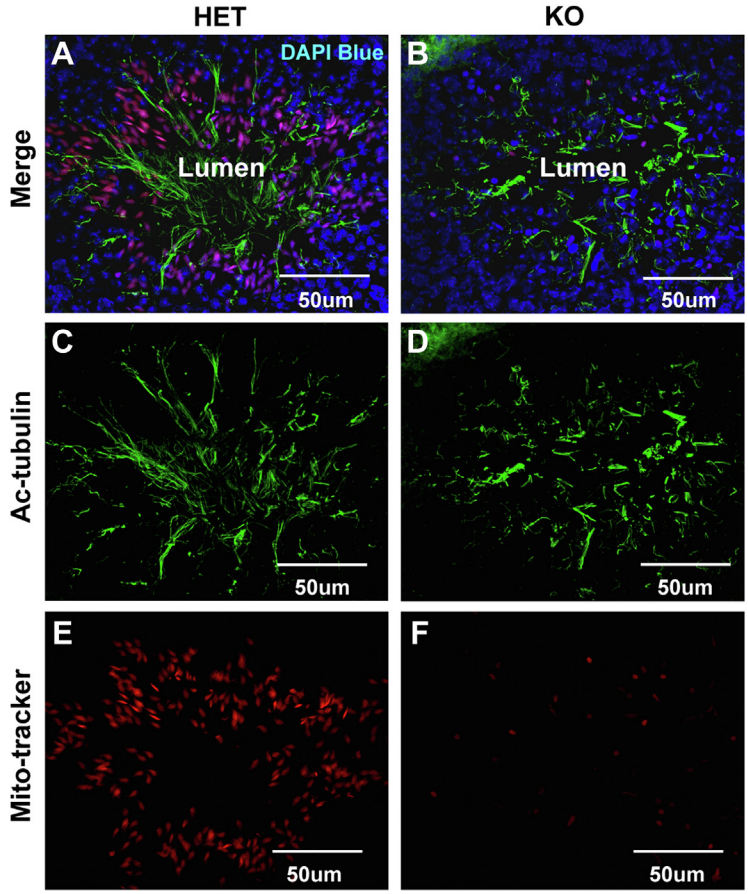

G

Protein	Structure
Ac-Tub	Axoneme
ODF2	Outer dense fiber
AKAP82	Fibrous sheath

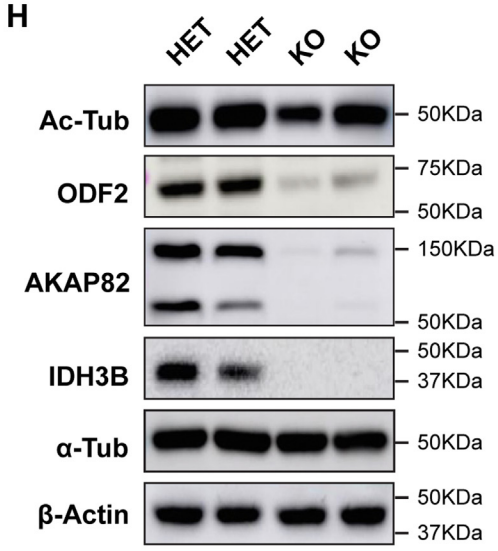

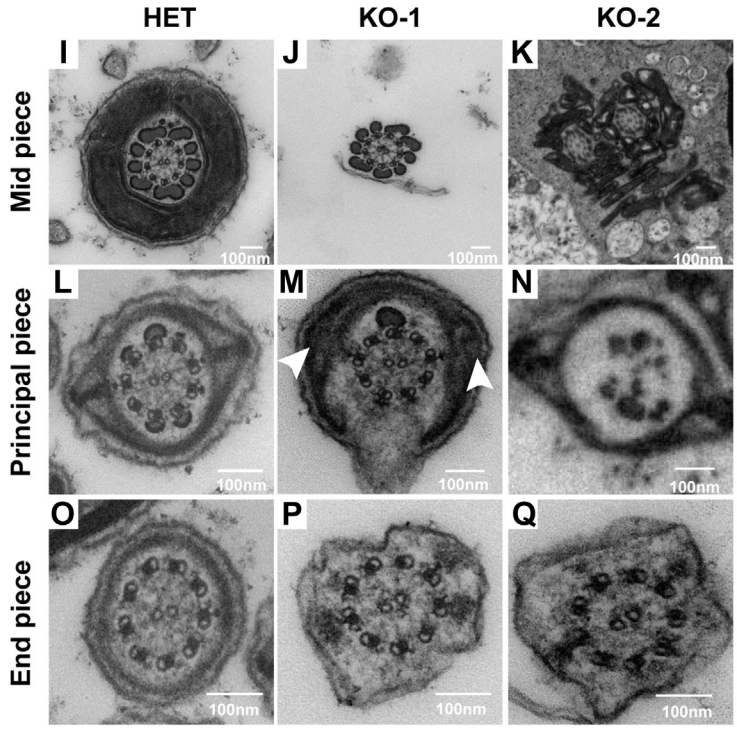

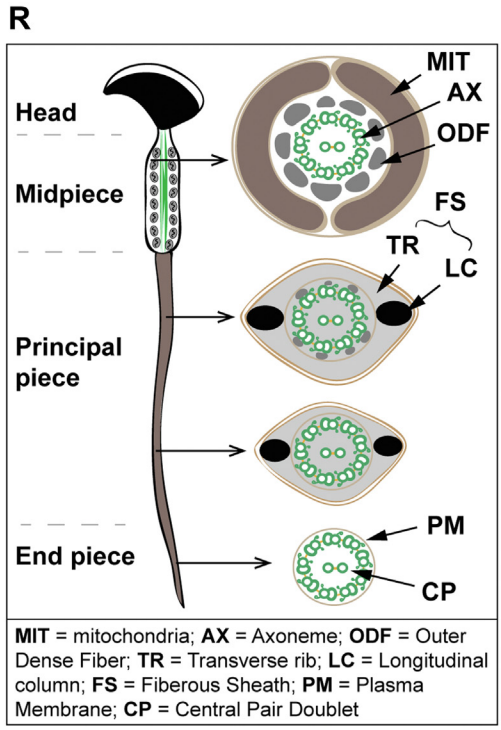

Figure 7. Flagellum biogenesis defects in *Idh3b* KO mice. *A–F*, immunofluorescent staining of axoneme and mitochondria in late-stage differentiating testicular tubule from mice at P50. *Red*, MitoTracker; *blue*, DAPI (4′,6-diamidino-2-phenylindole); *green*, acetyl-α-tubulin. *G*, table of proteins as structural components for flagellum integrity. Ac-tubulin, acetyl-α-tubulin; AKAP82, A-kinase anchor protein 82 kD; ODF2, outer dense fiber of sperm tails 2. *H*, Western blot analysis of listed proteins in testis from HET and KO mice at P50. β-Actin is adapted from Figure 6 and reused as internal standard. *I–Q*, ultrastructure analysis of different pieces of flagellum from mice at P50. *Arrowheads* pointed toward the longitudinal column. *R*, a schematic of flagellum structures. HET, heterozygous.

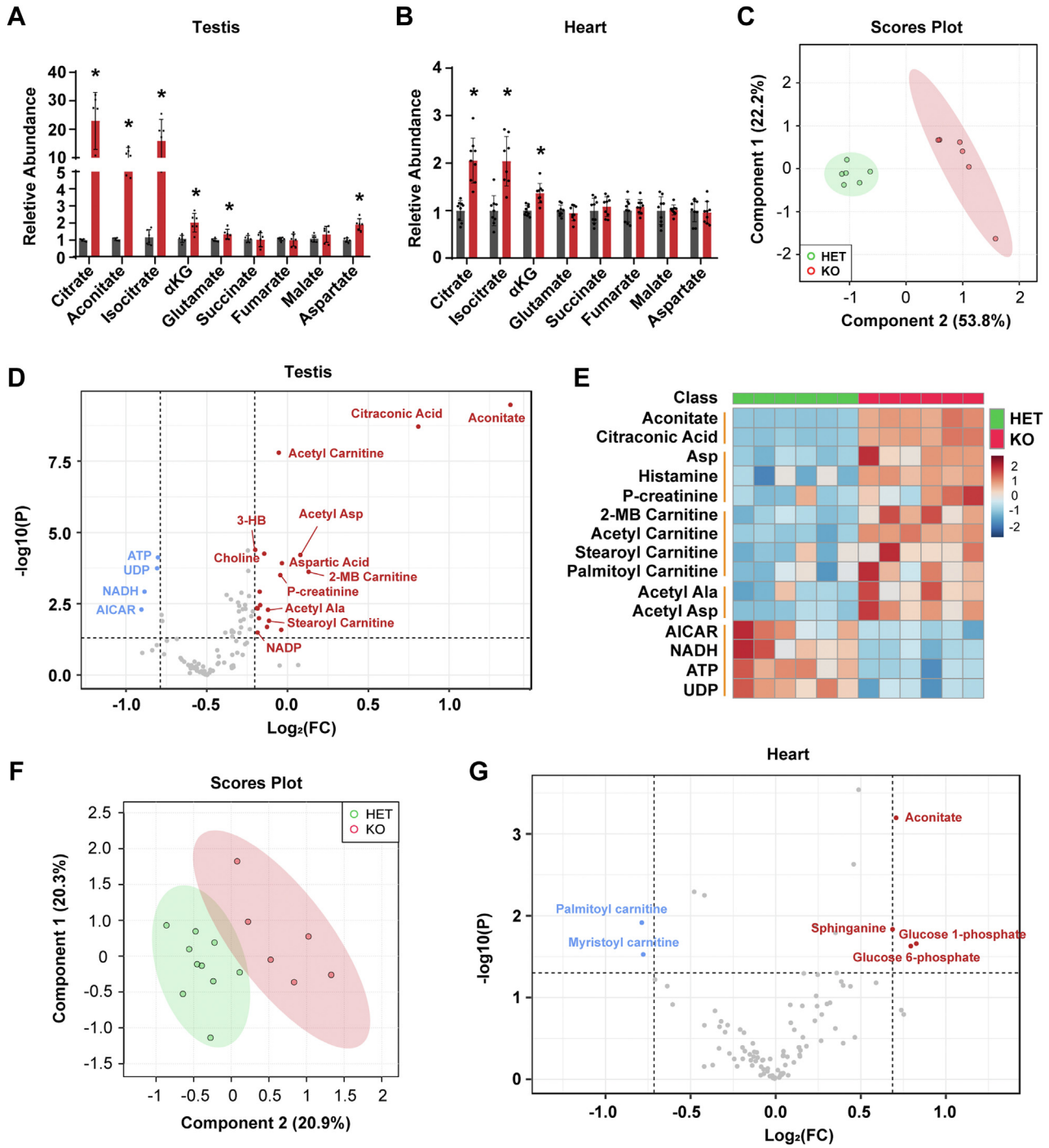

Figure 8. Loss of *Idh3b* dramatically disrupted cellular metabolism in testis but not the heart. *A*, fold change of TCA cycle metabolites in testis from KO mice at P50. N ≥ 6, *$p < 0.05$. *B*, fold change of TCA cycle metabolites in the heart from KO mice at P50. N ≥ 8, *$p < 0.05$. *C*, multivariant analysis of metabolomic study for testis by LC/MS. N = 6. *D*, volcano plot of metabolites from the testes by LC/MS. N ≥ 6, fold change ≥1.5, $p < 0.05$. *E*, heatmap for top 15 changed metabolites. N = 6, fold change ≥1.5, $p < 0.05$. *F*, multivariant analysis of metabolites from the heart. N ≥ 8. *G*, volcano plot of metabolites from the heart by LC/MS. N ≥ 8, fold change ≥1.5, $p < 0.05$. Data are all represented as mean ± SD; *t* test. TCA, TCA, tricarboxylic acid.

the massive accumulation of substrates probably exceeds the maximal rates of IDH1/2 for full compensation. To examine the impact of *Idh3b*-KO on the metabolome, we performed targeted metabolomics covering 206 metabolites in major metabolic pathways in glucose, amino acid, and nucleotide metabolism (Table S3). Multivariant analysis showed that the score plots of metabolites from the KO were well separated from the HET, demonstrating that the loss of *Idh3b* significantly alters testis metabolome (Fig. 8*C*). Citrate and isocitrate were not in the targeted metabolomics, but we found that citraconic acid (formed by the heating of citrate) and aconitate were substantially increased in the KO samples, consistent with the GC/MS results. Notably, multiple acylcarnitines, acetylated amino acids, the ketone body 3-hydroxybutyrate,

and phosphocreatine were increased in the KO testes, suggesting there is an energetic deficit (Fig. 8, *D* and *E*). Consistent with these results, ATP, NADH, and UDP were significantly decreased in testes from the KO mice (Fig. 8, *D* and *E*). However, the heart metabolome between the HET and KO was mostly overlapping, and high-energy metabolites, such as ATP, NADH, and phosphocreatine, were normal in the KO hearts (Fig. 8, *F* and *G*). Most acylcarnitines were normal or decreased rather than accumulated in the KO hearts. These results suggest that IDH3b is specifically required in testis for mitochondrial metabolism.

Discussion

In this study, we have found that IDH3B is essential for IDH3 activity in the retina, heart, brain, and testis. As a TCA cycle enzyme, IDH3 is important for maintaining the levels of citrate, isocitrate, and aconitate, especially in the testis. IDH3B is dispensable for visual function and photoreceptor survival. However, it is critical for testis metabolism and sperm development. The testis specifically requires IDH3B to maintain its mitochondrial bioenergetics and acrosome and flagella biogenesis during spermiogenesis.

The full activity of IDH3 requires the assembly and cooperation of αβ and αγ heterodimers. *In vitro* biochemical reconstitution of subunits shows that α, β, or γ subunit alone is nearly inactive, but αγ heterodimer exhibits activity that is weaker than the fully assembled enzyme (13). IDH3B plays a critical structural role in assembling the holoenzyme in the forms of heterotetramer or heterooctamer (14, 30). We found that IDH3B ablation almost completely abolishes IDH3 activity in different tissues (Fig. 1*D*), indicating that the β subunit is important for the assembly or stability of αγ heterodimer *in vivo*. These results are consistent with the finding in the larval salivary gland cells in *D. melanogaster* that the presumable *Idh3b* null allele blocks mitochondrial metabolism (24). However, it is still unclear why the loss of *Idh3b* alters the protein expression of other subunits in the testis but not the retina. It is possible that IDH3 subunits in the testis have their specific interactions and/or post-translational regulation that govern their protein stability, which has been discovered for protein subunits in other systems (31, 32).

All the *Idh3*-KO tissues that we measured showed an accumulation of precursors (citrate, isocitrate, and aconitate), particularly in the testis, but the level of the products (αKG and succinate) was unchanged or slightly increased. Under normal conditions, citrate from glucose, lipids, or amino acids is rapidly utilized through (1) TCA cycle by aconitase and IDH3, (2) IDH1 and IDH2, and (3) ATP citrate lyase to be cleaved into acetyl-CoA as acetyl group donor and oxaloacetate as a substrate for aspartate and malate. In addition to IDHs, αKG can also be produced from glutamate through multiple transaminases and glutamate dehydrogenase (33). It remains to be understood how these pathways compensate to maintain the levels of the products of the IDH3 reaction. The compensation among IDH isoforms is different in different tissues and cells (34–37). For example, IDH2 is capable of compensating mutated IDH1 in tumor cells under hypoxic conditions. However, IDH2 deficiency in mice is sufficient to cause mitochondrial dysfunction and cardiac hypertrophy (36, 37). Besides, IDH2 and IDH3 can compensate for each other in pancreatic beta cells to maintain insulin secretion, while in inner ears, IDH3 cannot compensate for the loss of IDH2, resulting in accelerated age-related hearing loss in male mice (34, 35). In testes from *Idh3*-KO mice, we observed an increase of aspartate, acylcarnitines, and acetylated amino acids, further suggesting the compensation of these pathways. Still, these compensations cannot maintain the levels of NADH, ATP, and other high-energy metabolites. Noteworthy, data from single-cell RNA-Seq databases for testis showed that the expression of IDH1 and IDH2 is much less abundant than IDH3A, IDH3B, and IDH3G in late spermatids (38, 39). Based on these findings, we speculate that IDH3 may be the primary dehydrogenase for mitochondrial NADH production in the testis.

IDH3 mutations have been correlated with inherited retinal degeneration (4, 15–17). Patients with *IDH3A* mutations showed an early onset (1–11 years old) of retinal degeneration, and patients with *IDH3B* mutation showed a late onset (30–50 years old) of retinal degeneration (4, 15–17). The loss of *Idh3a* in mice is embryonically lethal, and the mouse *Idh3a* E229K mutation leads to an early and rapid retinal degeneration (23). However, the loss of *Idh3b* in mice through an 8-bp deletion in exon 5 shows no retinal degeneration at P180 (23). This report is consistent with our findings that *Idh3b*-KO mice have normal vision up to P250, which is equivalent to 30 to 40 years of age in humans. It is possible that human *IDH3B* mutants may have an unknown malfunction such as gain of function and nonmetabolic function to cause retinal degeneration, which has been identified in mutations of other enzymes. For example, the mutations of inosine monophosphate dehydrogenase 1 (*IMPDH1*), a key enzyme in *de novo* nucleotide synthesis, cause severe retinal degeneration in patients, but 1-year-old *Impdh1* KO mice maintain normal retinal structure (40). The *Impdh1* mutants are proposed to reduce binding to nucleotide and association with polyribosomes (32). Another example is *IDH2*. Its mutations can gain a new function to generate 2-hydroxyglutarate, an oncometabolite in tumorigenesis (41). Interestingly, IDH3A has been reported to localize in the nucleus and interact with transcriptional factors to promote tumor growth (19). It is unknown whether IDH3B or its disease mutants moonlight similar other activities. Future study of the function of the mutant IDH3B proteins is warranted to elucidate the conundrum of retinal phenotypes in humans.

Why is IDH3B or IDH3 crucial for sperm development? There is a shift reliance of metabolism from glycolysis to TCA cycle during sperm development (42). The aerobic oxidation of lactate, glucose, pyruvate, and fatty acids through the TCA cycle is required to meet the high energetic demands in the maturation of spermatids (43–45). The TCA cycle enzymes are generally regarded as ubiquitous in nucleated cells for their housekeeping functions. However, the deficiencies of these enzymes, including fumarase, succinate dehydrogenase, and αKG dehydrogenase, show tissue-specific impairment (46–48).

Our findings demonstrate that IDH3B is specifically required for IDH3 activity, mitochondrial metabolism, and spermiogenesis. IDH3B proteins are underexpressed in low motile spermatozoa or spermatozoa from infertile men with varicocele (21). IDH inhibitor can block sperm capacitation and inhibit acrosome reaction in boar spermatozoa (49). Intriguingly, Gossypol, a natural antifertility agent for males, causes specific mitochondrial damage in the tails of spermatozoa (50, 51), which has a similar phenotype to the *Idh3b*-KO mice. The block of IDH3 may be attributed to its induction of male infertility, as gossypol has been a known inhibitor of NAD-linked dehydrogenase including IDH3 (52). The environmental contaminant tributyltin, known to impair sperm maturation in the vertebrate (53, 54), is also a sensitive inhibitor of IDH3 (55).

The IDH3 reaction controls the levels of key metabolites (citrate, NADH, and ATP), which are essential for biosynthesis, cell signaling, and bioenergetics during sperm development (56–58). Besides the TCA cycle, citrate is an important source of acetyl-CoA, a substrate for *de novo* lipid synthesis and protein acetylation. During sperm differentiation, different compositions of lipid species are required to generate lipid-rich organelles like acrosome and flagellum (59). Compared with immature spermatids, mature sperms have high amounts of polyunsaturated fatty acids (PUFAs) (59). The disruption of key enzymes in PUFA synthesis such as acyl-CoA synthetase 6 and delta-6 desaturase can arrest spermiogenesis, resulting in male infertility (60–63) with similar phenotypes to the *Idh3b*-KO mice. In addition, NADH is a required cofactor for key desaturases including delta-6 desaturases in PUFA metabolism (64). Also, the acetylation of histone tightly regulates sperm development, especially during the late-stage differentiation (65–68). During spermiogenesis, matured spermatozoa acquire a highly condensed genome by replacing 95% of histone into protamine, a small protein facilitating chromatin condensation. The disruption of histone acetylation impairs histone replacement and causes defects in sperm development (65, 69). It will be interesting to investigate how IDH3B regulates these biosynthesis pathways and acetylation status in future studies.

In conclusion, our studies show a tissue-specific requirement of IDH3B on modulating mitochondrial metabolism and tissue functions. IDH3B is required for testis metabolism and proper sperm development.

Limitations of the study

Because of limited resource, full characterizations of other tissues such as heart and brain are not available in this study. Mitochondrial structure is critical to support metabolism, and it will be interesting to investigate whether and how IDH3B deletion influences mitochondrial structure and dynamics in testes and other tissues. Citrate is a precursor and key regulator in *de novo* lipogenesis. The influence of IDH3 KO on *de novo* lipogenesis in the testes remains to be addressed. Finally, each tissue has different preferences in substrate utilization. Future studies with tracing of major substrates *in vivo* and *ex vivo* using our animal model should provide insights on the importance of IDH3 in substrate utilization in different tissues.

Experimental procedures

All the chemicals and reagents are detailed in the *Key Resource Table* (Table S2).

Animals

Idh3b HET male mice were purchased from the Jackson Laboratory (stock number: 042302-JAX) and crossed with WT female mice (C57BL/6J) to transmit the Idh3b-deficient allele to their offspring. The HET males were bred with *Idh3b* homozygous KO females to generate *Idh3b*-KO mice and HET littermate controls for experiments. Mouse genotyping was accomplished by Transnetyx, Inc using provided primers (see details in Table S1). Both sexes were used in visual studies but only males for sperm studies. The mouse experiments were performed in accordance with the National Institutes of Health guidelines and the protocol approved by the Institutional Animal Care and Use Committee of West Virginia University.

Western blot

The tissues were lysed in radioimmunoprecipitation assay buffer supplemented with protease and phosphatase inhibitors at 5 mg/ml concentration. The supernatant containing proteins was collected after centrifuging tissue lysates at 12,000 rpm in 4 °C. Protein concentration was determined by the bicinchoninic acid protein assay kit, and 20 μg protein samples were boiled and loaded onto SDS-PAGE gels. The gels were transferred to 0.22 μm nitrocellulose membranes and blocked with 5% nonfat milk in 1× Tris-buffered saline containing 0.1% Tween-20. The membranes were incubated with primary antibodies (see details in Table S2) at 4 °C overnight. After three washes (15, 5, and 5 min) with 1× PBS containing 0.1% Tween-20, the membranes were incubated with a rabbit or mouse secondary antibody conjugated with horseradish peroxidase (1:2000 dilution) or Alexa Fluor 680 (1:10,000 dilution) for 1 h, followed by three washes (15, 5, and 5 min) with PBS with Tween-20. A chemiluminescence reagent kit was used to visualize protein bands with horseradish peroxidase secondary antibodies. Western blot using Alexa Fluor secondary antibody were performed as previously reported (70).

Enzyme activity measurement

Samples were harvested from mice at P50 and homogenized in 50 mM Hepes/KOH buffer (pH 7.4) containing 1% Triton, 1 mM EDTA, 10% glycerol, and 5 mg/ml protease and phosphatase inhibitors. After centrifuged at 12,000 rpm at 4 °C, the supernatants were assayed for protein concentrations, and 50 μg proteins were loaded for enzymatic activity assays. IDH3 activity was determined by incubating the protein extracts in the assay buffer containing 2 mM Mn^{2+}, 2 mM NAD, and 10 mM isocitrate at 37 °C in a plate reader and monitoring the

production of NADH continuously for 4 h at 340 nm wavelength. IDH1 and IDH2 activities were determined by monitoring the production of NADPH at 340 nm wavelength for 4 h after incubation with assay buffer containing 1 mM Mg^{2+}, 1 mM NADP, and different concentrations of isocitrate (0, 1, 2, 3, 4, and 10 mM) at 37 °C. No enzyme controls were used as blank controls for each sample. Standard curves of NADH and NADPH were measured simultaneously for calculating the concentration of NADH and NADPH.

OCT

OCT was conducted as previously described (70). Mice were anesthetized with 1.5% isoflurane in a chamber and then received constant isoflurane during OCT *via* a nose cone. Both pupils were diluted before OCT measurement by applying one drop of 1:1 mixture of 2.5% phenylephrine hydrochloride and 1% tropicamide. To avoid cataract, each eye was applied a drop of GenTeal lubricant eye gel (Alcon) right after the dilation, and the body temperature of mice was maintained by a heating platform. Cross-sectional images of the retina were taken using the Bioptigen R-series spectral domain ophthalmic imaging system (Bioptigen, Inc), and the thickness of each layer was analyzed as previously described (70, 71).

ERG

Mice were dark-adapted overnight before recording ERG using Celeris D430 rodent ERG testing system (Diagnosys). Under dim red-light illumination, mice were anesthetized, and eyes were dilated as previously described (70). Scotopic recordings were elicited using light flashes at increasing intensities (0.004, 0.01, 0.063, 0.16, 0.36, 0.8, 1.26, 4, and 10 cd s/m^2). The photopic response was elicited with increasing flash intensities (1.26, 4, 10, and 20 cd s/m^2) after a short light adaptation with continuous background light.

H&E staining and analysis

The preparation and staining for eye, testis, and cauda epididymis were performed as reported before (70). The tissues were fixed, paraffin sectioned, and stained with H&E. The slides were imaged under a Nikon C2 confocal microscope, and the thickness of outer segment and inner segment in the retina was measured by ImageJ (National Institutes of Health) at six different positions of the retina as described before (70). For testis, 20 seminiferous tubules at four quadrants of testes sections were randomly selected and quantified for the number of sperm cells at different developmental stages.

Periodic acid-Schiff staining and analysis

Similar to H&E staining, testes were embedded in paraffin and sectioned at 4 to 6 microns. The sections were stained with 1% periodic acid, McManus Schiff stain reagent, and Gill III hematoxylin. The stained sections were imaged by a confocal microscope and staged for sperm differentiation based on acrosomal morphology.

Sperm cell video recording and counting

For sperm cell video, we dissected cauda epididymis in 1 ml α minimum essential medium and recorded the sperm movement using EVOS FL Auto 2 Cell Imaging System. To count the number of sperm cells, we sacrificed the mice and dissected the cauda epididymis in 1 ml PBS and spun the mix at 1500 rpm for 3 min. The aggregates were fixed in 4% paraformaldehyde, resuspended in PBS, and counted using a hemocytometer.

Immunofluorescence

Testes were immediately fixed in 4% paraformaldehyde for 24 h at 4 °C and rinsed by PBS, dehydrated by 20% sucrose, and then cryopreserved in optimal cutting temperature compound to section at 10 μm for immunostaining. Sections were washed with PBS containing 1% Triton X-100 for three times and incubated in blocking buffer (10% goat serum with 0.5% Triton) at room temperature for an hour before staining with antibodies or dyes. Primary antibody control and negative controls with secondary antibody–only staining were applied for all immunofluorescent studies (Figs. S6 and S7). Fluorescent sections were imaged by a Nikon C2 confocal microscope system.

TEM

Testes were cut into half and fixed in 4% glutaraldehyde (Electron Microscopy Sciences) for 30 min, then sliced into ~1 mm^3 pieces, and continued to be fixed in the same buffer overnight at 4 °C. The prefixed testes were washed 5× 5 min in 0.1 M cacodylate buffer and postfixed in osmium ferrocyanide for 1 h on ice. Next, the testes were incubated in a 1% thiocarbohydrazide solution for 20 min following by 2% osmium tetroxide for 30 min at room temperature. The tissues were en bloc stained in 1% uranyl acetate, (aqueous), overnight in the refrigerator and en bloc stained in Walton's lead aspartate for 30 min at 60 °C, the second day. Then, the testes were dehydrated in ice-cold 30, 50, 70, and 95% ethanol alcohol and infiltrated in a 1:1 mixture of propylene oxide:Durcupan resin, for 2 h and then overnight infiltration in fresh Durcupan. The next day, the testes were placed in fresh Durcupan for 2 h, positioned in flat embedding molds, and polymerized in a 60 °C oven for 2 days. About 80 nm sections were cut on a Leica EM UC7 ultramicrotome, and sections were viewed on a JEOL 1230 TEM at 80 KV.

Steady-state metabolomics and ^{13}C-labeled metabolite analysis by GC/MS

Steady-state metabolomics and ^{13}C-labeled metabolite analysis for retina were performed as described in detail before (70). The metabolites were extracted in 80% cold methanol (v/v), dried, and derivatized by methoxymine hydrochloride followed by *N*-(*tert*-butyldimethylsilyl)-*N*-methyltrifluoroacetamide. An Agilent 7890B/5977B GC/MS was used for GC separation and analysis of metabolites. The data were analyzed by Agilent MassHunter Quantitative Analysis Software, and natural abundance was corrected by ISOCOR

software (freely available online: https://isocor.readthedocs.io/en/latest/).

Targeted metabolomics by LC MS/MS

Targeted metabolomics by LC MS/MS was performed as reported before (70). Briefly, metabolites from testes were extracted in 80% cold methanol and analyzed by a Shimadzu LC Nexera X2 UHPLC coupled with a QTRAP 5500 LC MS/MS (AB Sciex) in multiple reaction monitoring mode. Each metabolite was tuned with standards for optimal transitions (see details in Table S3). The extracted multiple reaction monitoring peaks were integrated using MultiQuant 3.0.2 software (AB Sciex).

Statistics

The significance of differences between means was determined by unpaired two-tailed t tests using GraphPad Prism 9.0 (GraphPad Software, Inc). Only $p < 0.05$ was considered to be significant. All data are presented as the mean ± SD. Multivariate analysis of metabolomics data was performed with a supervised classification model partial least-squares discriminant analysis after Pareto scaling using MetaboAnalyst 5.0, an online free software from Xia Lab at the McGill University (https://www.metaboanalyst.ca/). Volcano plot ($p < 0.05$ and fold change >1.5) was performed to analyze the changes of specific metabolites using MetaboAnalyst 5.0.

Data availability

GC/MS and LC/MS data generated in this study were provided in the supporting information. Source data are provided with this article.

Supporting information—This article contains supporting information.

Acknowledgments—This work was supported by funds for Core facilities P20 grant GM103434 (WV INBRE grant) and WVCTSI grant GM104942. We thank Dr Roberta Leonardi for mouse secondary antibody, Dr Saravanan Kolandaivelu for GM130 antibody, and Dr Visvanathan Ramamurthy for acetyl-tubulin antibody.

Author contributions—S. Z. and J. D. conceptualization; J. H., R. X., Yek W., Yim W, R. M., E. P., D. K., M. Y., B. W., C. Z., J. S., and J. D. investigation; S. Z. and J. D. writing–original draft; J. D. supervision; J. D. funding acquisition.

Funding and additional information—This work was supported by the National Institutes of Health grant (EY031324; to J. D.), EY032462 (to J. D.), Bright Focus Foundation grant (M2020141; to J. D.), the Retina Research Foundation (to J. D.). The content is solely the responsibility of the authors and does not necessarily represent the official views of the National Institutes of Health.

Conflict of interest—The authors declare that they have no conflicts of interest with the contents of this article.

Abbreviations—The abbreviations used are: αKG, α-ketoglutarate; ERG, electroretinogram; IDH, isocitrate dehydrogenase; IMPDH1, inosine monophosphate dehydrogenase 1; OCT, optical coherence tomography; PUFA, polyunsaturated fatty acid; TCA, tricarboxylic acid; TEM, transmission electron microscope.

References

1. Martinez-Reyes, I., and Chandel, N. S. (2020) Mitochondrial TCA cycle metabolites control physiology and disease. *Nat. Commun.* **11**, 102
2. Ryan, D. G., Murphy, M. P., Frezza, C., Prag, H. A., Chouchani, E. T., O'Neill, L. A., *et al.* (2019) Coupling Krebs cycle metabolites to signalling in immunity and cancer. *Nat. Metab.* **1**, 16–33
3. Pavlova, N. N., and Thompson, C. B. (2016) The Emerging hallmarks of cancer metabolism. *Cell Metab.* **23**, 27–47
4. Hartong, D. T., Dange, M., McGee, T. L., Berson, E. L., Dryja, T. P., and Colman, R. F. (2008) Insights from retinitis pigmentosa into the roles of isocitrate dehydrogenases in the Krebs cycle. *Nat. Genet.* **40**, 1230–1234
5. Park, Y. J., and Pang, M. G. (2021) Mitochondrial functionality in male fertility: from spermatogenesis to fertilization. *Antioxidants (Basel)* **10**, 98
6. Koh, H. J., Lee, S. M., Son, B. G., Lee, S. H., Ryoo, Z. Y., Chang, K. T., *et al.* (2004) Cytosolic NADP+-dependent isocitrate dehydrogenase plays a key role in lipid metabolism. *J. Biol. Chem.* **279**, 39968–39974
7. Wise, D. R., Ward, P. S., Shay, J. E., Cross, J. R., Gruber, J. J., Sachdeva, U. M., *et al.* (2011) Hypoxia promotes isocitrate dehydrogenase-dependent carboxylation of alpha-ketoglutarate to citrate to support cell growth and viability. *Proc. Natl. Acad. Sci. U. S. A.* **108**, 19611–19616
8. Jiang, L., Shestov, A. A., Swain, P., Yang, C., Parker, S. J., Wang, Q. A., *et al.* (2016) Reductive carboxylation supports redox homeostasis during anchorage-independent growth. *Nature* **532**, 255–258
9. Du, J., Yanagida, A., Knight, K., Engel, A. L., Vo, A. H., Jankowski, C., *et al.* (2016) Reductive carboxylation is a major metabolic pathway in the retinal pigment epithelium. *Proc. Natl. Acad. Sci. U. S. A.* **113**, 14710–14715
10. Gabriel, J. L., Zervos, P. R., and Plaut, G. W. (1986) Activity of purified NAD-specific isocitrate dehydrogenase at modulator and substrate concentrations approximating conditions in mitochondria. *Metabolism* **35**, 661–667
11. Sazanov, L. A., and Jackson, J. B. (1994) Proton-translocating transhydrogenase and NAD- and NADP-linked isocitrate dehydrogenases operate in a substrate cycle which contributes to fine regulation of the tricarboxylic acid cycle activity in mitochondria. *FEBS Lett.* **344**, 109–116
12. Bzymek, K. P., and Colman, R. F. (2007) Role of alpha-Asp181, beta-Asp192, and gamma-Asp190 in the distinctive subunits of human NAD-specific isocitrate dehydrogenase. *Biochemistry* **46**, 5391–5397
13. Ehrlich, R. S., and Colman, R. F. (1983) Separation, recombination, and characterization of dissimilar subunits of the DPN-dependent isocitrate dehydrogenase from pig heart. *J. Biol. Chem.* **258**, 7079–7086
14. Ma, T., Peng, Y., Huang, W., Liu, Y., and Ding, J. (2017) The beta and gamma subunits play distinct functional roles in the alpha2betagamma heterotetramer of human NAD-dependent isocitrate dehydrogenase. *Sci. Rep.* **7**, 41882
15. Sun, W., and Zhang, Q. (2018) A novel variant in IDH3A identified in a case with Leber congenital amaurosis accompanied by macular pseudocoloboma. *Ophthalmic Genet.* **39**, 662–663
16. Peter, V. G., Nikopoulos, K., Quinodoz, M., Granse, L., Farinelli, P., Superti-Furga, A., *et al.* (2019) A novel missense variant in IDH3A causes autosomal recessive retinitis pigmentosa. *Ophthalmic Genet.* **40**, 177–181
17. Pierrache, L. H. M., Kimchi, A., Ratnapriya, R., Roberts, L., Astuti, G. D. N., Obolensky, A., *et al.* (2017) Whole-exome sequencing identifies biallelic IDH3A variants as a cause of retinitis pigmentosa accompanied by pseudocoloboma. *Ophthalmology* **124**, 992–1003

18. Zenteno, J. C., Garcia-Montano, L. A., Cruz-Aguilar, M., Ronquillo, J., Rodas-Serrano, A., Aguilar-Castul, L., *et al.* (2020) Extensive genic and allelic heterogeneity underlying inherited retinal dystrophies in Mexican patients molecularly analyzed by next-generation sequencing. *Mol. Genet. Genomic Med.* **8**. https://doi.org/10.1002/mgg3.1044
19. Liu, X., Qiao, Y., Ting, X., and Si, W. (2020) Isocitrate dehydrogenase 3A, a rate-limiting enzyme of the TCA cycle, promotes hepatocellular carcinoma migration and invasion through regulation of MTA1, a core component of the NuRD complex. *Am. J. Cancer Res.* **10**, 3212–3229
20. May, J. L., Kouri, F. M., Hurley, L. A., Liu, J., Tommasini-Ghelfi, S., Ji, Y., *et al.* (2019) IDH3alpha regulates one-carbon metabolism in glioblastoma. *Sci. Adv.* **5**, eaat0456
21. Agarwal, A., Sharma, R., Samanta, L., Durairajanayagam, D., and Sabanegh, E. (2016) Proteomic signatures of infertile men with clinical varicocele and their validation studies reveal mitochondrial dysfunction leading to infertility. *Asian J. Androl.* **18**, 282–291
22. Moscatelli, N., Lunetti, P., Braccia, C., Armirotti, A., Pisanello, F., De Vittorio, M., *et al.* (2019) Comparative proteomic analysis of proteins involved in bioenergetics pathways associated with human sperm motility. *Int. J. Mol. Sci.* **20**, 3000
23. Findlay, A. S., Carter, R. N., Starbuck, B., McKie, L., Novakova, K., Budd, P. S., *et al.* (2018) Mouse Idh3a mutations cause retinal degeneration and reduced mitochondrial function. *Dis. Model. Mech.* **11**, dmm036426
24. Duncan, D. M., Kiefel, P., and Duncan, I. (2017) Mutants for Drosophila isocitrate dehydrogenase 3b are defective in mitochondrial function and larval cell death. *G3 (Bethesda)* **7**, 789–799
25. Du, J., Cleghorn, W., Contreras, L., Linton, J. D., Chan, G. C., Chertov, A. O., *et al.* (2013) Cytosolic reducing power preserves glutamate in retina. *Proc. Natl. Acad. Sci. U. S. A.* **110**, 18501–18506
26. Lindsay, K. J., Du, J., Sloat, S. R., Contreras, L., Linton, J. D., Turner, S. J., *et al.* (2014) Pyruvate kinase and aspartate-glutamate carrier distributions reveal key metabolic links between neurons and glia in retina. *Proc. Natl. Acad. Sci. U. S. A.* **111**, 15579–15584
27. Audouard, C., and Christians, E. (2011) Hsp90beta1 knockout targeted to male germline: a mouse model for globozoospermia. *Fertil. Steril.* **95**. https://doi.org/10.1016/j.fertnstert.2010.12.006
28. Yao, R., Ito, C., Natsume, Y., Sugitani, Y., Yamanaka, H., Kuretake, S., *et al.* (2002) Lack of acrosome formation in mice lacking a Golgi protein, GOPC. *Proc. Natl. Acad. Sci. U. S. A.* **99**, 11211–11216
29. Tang, A., Yan, Q., Sun, L., Diao, R., Yu, Z., Zhang, Z., *et al.* (2012) Developmental expression of ACRV1 in humans and mice. *Andrologia* **44**, 16–22
30. Sun, P., Liu, Y., Ma, T., and Ding, J. (2020) Structure and allosteric regulation of human NAD-dependent isocitrate dehydrogenase. *Cell Discov.* **6**, 94
31. Arlow, T., Kim, J., Haye-Bertolozzi, J. E., Martinez, C. B., Fay, C., Zorensky, E., *et al.* (2021) MutSalpha mismatch repair protein stability is governed by subunit interaction, acetylation, and ubiquitination. *G3 (Bethesda)* **11**, jkaa065
32. Plank, T., Toole, C., and Anderson, L. K. (1995) Subunit interactions and protein stability in the cyanobacterial light-harvesting proteins. *J. Bacteriol.* **177**, 6798–6803
33. Xu, R., Ritz, B. K., Wang, Y., Huang, J., Zhao, C., Gong, K., *et al.* (2020) The retina and retinal pigment epithelium differ in nitrogen metabolism and are metabolically connected. *J. Biol. Chem.* **295**, 2324–2335
34. White, K., Kim, M. J., Han, C., Park, H. J., Ding, D., Boyd, K., *et al.* (2018) Loss of IDH2 Accelerates age-related hearing loss in male mice. *Sci. Rep.* **8**, 5039
35. MacDonald, M. J., Brown, L. J., Longacre, M. J., Stoker, S. W., Kendrick, M. A., and Hasan, N. M. (2013) Knockdown of both mitochondrial isocitrate dehydrogenase enzymes in pancreatic beta cells inhibits insulin secretion. *Biochim. Biophys. Acta* **1830**, 5104–5111
36. Ku, H. J., Ahn, Y., Lee, J. H., Park, K. M., and Park, J. W. (2015) IDH2 deficiency promotes mitochondrial dysfunction and cardiac hypertrophy in mice. *Free Radic. Biol. Med.* **80**, 84–92
37. Zhang, Y., Lv, W., Li, Q., Wang, Q., Ru, Y., Xiong, X., *et al.* (2019) IDH2 compensates for IDH1 mutation to maintain cell survival under hypoxic conditions in IDH1mutant tumor cells. *Mol. Med. Rep.* **20**, 1893–1900
38. Shami, A. N., Zheng, X., Munyoki, S. K., Ma, Q., Manske, G. L., Green, C. D., *et al.* (2020) Single-cell RNA sequencing of human, macaque, and mouse testes uncovers conserved and divergent features of mammalian spermatogenesis. *Dev. Cell* **54**, 529–547.e512
39. Guo, J., Grow, E. J., Mlcochova, H., Maher, G. J., Lindskog, C., Nie, X., *et al.* (2018) The adult human testis transcriptional cell atlas. *Cell Res.* **28**, 1141–1157
40. Aherne, A., Kennan, A., Kenna, P. F., McNally, N., Lloyd, D. G., Alberts, I. L., *et al.* (2004) On the molecular pathology of neurodegeneration in IMPDH1-based retinitis pigmentosa. *Hum. Mol. Genet.* **13**, 641–650
41. Ye, D., Guan, K. L., and Xiong, Y. (2018) Metabolism, activity, and targeting of D- and L-2-hydroxyglutarates. *Trends Cancer* **4**, 151–165
42. Bajpai, M., Gupta, G., and Setty, B. S. (1998) Changes in carbohydrate metabolism of testicular germ cells during meiosis in the rat. *Eur. J. Endocrinol.* **138**, 322–327
43. Bajpai, M., Gupta, G., Jain, S. K., and Setty, B. S. (1998) Lipid metabolising enzymes in isolated rat testicular germ cells and changes associated with meiosis. *Andrologia* **30**, 311–315
44. Boussouar, F., and Benahmed, M. (2004) Lactate and energy metabolism in male germ cells. *Trends Endocrinol. Metab.* **15**, 345–350
45. Mita, M., and Hall, P. F. (1982) Metabolism of round spermatids from rats: lactate as the preferred substrate. *Biol. Reprod.* **26**, 445–455
46. Rustin, P., Bourgeron, T., Parfait, B., Chretien, D., Munnich, A., and Rotig, A. (1997) Inborn errors of the Krebs cycle: a group of unusual mitochondrial diseases in human. *Biochim. Biophys. Acta* **1361**, 185–197
47. Briere, J. J., Favier, J., El Ghouzzi, V., Djouadi, F., Benit, P., Gimenez, A. P., *et al.* (2005) Succinate dehydrogenase deficiency in human. *Cell Mol. Life Sci.* **62**, 2317–2324
48. Broeks, M. H., Shamseldin, H. E., Alhashem, A., Hashem, M., Abdulwahab, F., Alshedi, T., *et al.* (2019) MDH1 deficiency is a metabolic disorder of the malate-aspartate shuttle associated with early onset severe encephalopathy. *Hum. Genet.* **138**, 1247–1257
49. Breininger, E., Dubois, D., Pereyra, V. E., Rodriguez, P. C., Satorre, M. M., and Cetica, P. D. (2017) Participation of phosphofructokinase, malate dehydrogenase and isocitrate dehydrogenase in capacitation and acrosome reaction of boar spermatozoa. *Reprod. Domest. Anim.* **52**, 731–740
50. Randel, R. D., Chase, C. C., Jr., and Wyse, S. J. (1992) Effects of gossypol and cottonseed products on reproduction of mammals. *J. Anim. Sci.* **70**, 1628–1638
51. Qian, S. Z., and Wang, Z. G. (1984) Gossypol: a potential antifertility agent for males. *Annu. Rev. Pharmacol. Toxicol.* **24**, 329–360
52. Ikeda, M. (1990) Inhibition kinetics of NAD-linked enzymes by gossypol acetic acid. *Andrologia* **22**, 409–416
53. Lan, X. R., Li, Y. W., Chen, Q. L., Shen, Y. J., and Liu, Z. H. (2020) Tributyltin impaired spermatogenesis and reproductive behavior in male zebra fi sh. *Aquat. Toxicol.* **224**, 105503
54. Yan, F., Chen, Y., Zuo, Z., Chen, Y., Yang, Z., and Wang, C. (2009) Effects of tributyltin on epididymal function and sperm maturation in mice. *Environ. Toxicol. Pharmacol.* **28**, 19–24
55. Yamada, S., Kotake, Y., Demizu, Y., Kurihara, M., Sekino, Y., and Kanda, Y. (2014) NAD-dependent isocitrate dehydrogenase as a novel target of tributyltin in human embryonic carcinoma cells. *Sci. Rep.* **4**, 5952
56. Hudry, B., de Goeij, E., Mineo, A., Gaspar, P., Hadjieconomou, D., Studd, C., *et al.* (2019) Sex differences in intestinal carbohydrate metabolism promote food intake and sperm maturation. *Cell* **178**, 901–918.e916
57. Yu, J., Chen, B., Zheng, B., Qiao, C., Chen, X., Yan, Y., *et al.* (2019) ATP synthase is required for male fertility and germ cell maturation in Drosophila testes. *Mol. Med. Rep.* **19**, 1561–1570
58. Galimov, S. N., Gromenko, J. Y., Bulygin, K. V., Galimov, K. S., Galimova, E. F., and Sinelnikov, M. Y. (2021) The level of secondary messengers and the redox state of NAD(+)/NADH are associated with sperm quality in infertility. *J. Reprod. Immunol.* **148**, 103383
59. Lenzi, A., Gandini, L., Maresca, V., Rago, R., Sgro, P., Dondero, F., *et al.* (2000) Fatty acid composition of spermatozoa and immature germ cells. *Mol. Hum. Reprod.* **6**, 226–231
60. Hale, B. J., Fernandez, R. F., Kim, S. Q., Diaz, V. D., Jackson, S. N., Liu, L., *et al.* (2019) Acyl-CoA synthetase 6 enriches seminiferous tubules with the omega-3 fatty acid docosahexaenoic acid and is required for male fertility in the mouse. *J. Biol. Chem.* **294**, 14394–14405

61. Shishikura, K., Kuroha, S., Matsueda, S., Iseki, H., Matsui, T., Inoue, A., *et al.* (2019) Acyl-CoA synthetase 6 regulates long-chain polyunsaturated fatty acid composition of membrane phospholipids in spermatids and supports normal spermatogenic processes in mice. *FASEB J.* **33**, 14194–14203
62. Roqueta-Rivera, M., Abbott, T. L., Sivaguru, M., Hess, R. A., and Nakamura, M. T. (2011) Deficiency in the omega-3 fatty acid pathway results in failure of acrosome biogenesis in mice. *Biol. Reprod.* **85**, 721–732
63. Stroud, C. K., Nara, T. Y., Roqueta-Rivera, M., Radlowski, E. C., Lawrence, P., Zhang, Y., *et al.* (2009) Disruption of FADS2 gene in mice impairs male reproduction and causes dermal and intestinal ulceration. *J. Lipid Res.* **50**, 1870–1880
64. Kim, W., Deik, A., Gonzalez, C., Gonzalez, M. E., Fu, F., Ferrari, M., *et al.* (2019) Polyunsaturated fatty acid desaturation is a mechanism for glycolytic NAD(+) recycling. *Cell Metab.* **29**, 856–870.e857
65. Dong, Y., Isono, K. I., Ohbo, K., Endo, T. A., Ohara, O., Maekawa, M., *et al.* (2017) EPC1/TIP60-Mediated histone acetylation facilitates spermiogenesis in mice. *Mol. Cell Biol.* **37**
66. Luense, L. J., Donahue, G., Lin-Shiao, E., Rangel, R., Weller, A. H., Bartolomei, M. S., *et al.* (2019) Gcn5-Mediated histone acetylation governs nucleosome dynamics in spermiogenesis. *Dev. Cell* **51**, 745–758.e746
67. Kavarthapu, R., Anbazhagan, R., Sharma, A. K., Shiloach, J., and Dufau, M. L. (2020) Linking phospho-gonadotropin regulated testicular RNA helicase (GRTH/DDX25) to histone ubiquitination and acetylation essential for spermatid development during spermiogenesis. *Front. Cell Dev. Biol.* **8**, 310
68. Yin, H., Kang, Z., Zhang, Y., Gong, Y., Liu, M., Xue, Y., *et al.* (2021) HDAC3 controls male fertility through enzyme-independent transcriptional regulation at the meiotic exit of spermatogenesis. *Nucl. Acids Res.* **49**, 5106–5123
69. Bell, E. L., Nagamori, I., Williams, E. O., Del Rosario, A. M., Bryson, B. D., Watson, N., *et al.* (2014) SirT1 is required in the male germ cell for differentiation and fecundity in mice. *Development* **141**, 3495–3504
70. Grenell, A., Wang, Y., Yam, M., Swarup, A., Dilan, T. L., Hauer, A., *et al.* (2019) Loss of MPC1 reprograms retinal metabolism to impair visual function. *Proc. Natl. Acad. Sci. U. S. A.* **116**, 3530–3535
71. Ferguson, L. R., Dominguez, J. M., 2nd, Balaiya, S., Grover, S., and Chalam, K. V. (2013) Retinal thickness normative data in wild-type mice using customized miniature SD-OCT. *PLoS One* **8**, e67265